RESEARCH ARTICLE

# Fracturing Effectiveness Evaluation Based on Flowback Data Using Pressure Transient Testing

**Luo Tian**[1,2], **Qiushi Zhang**[2,*], **Xingcai Li**[3] **and Cunlei Li**[2]

[1] School of Energy and Power Engineering, Xi'an Jiaotong University, Xi'an 710049, China
[2] College of Petroleum and Natural Gas Engineering, Liaoning University of Petrochemical Technology, Fushun 113001, China
[3] China Petroleum Group Great Wall Drilling Engineering Co., Ltd., Liaoning, China

## Abstract

**This study addresses fracturing performance evaluation during shale oil well flowback by developing a seepage flowback mathematical model and a water-phase evaluation framework. A method calculating effective fracture pore volume via flowback water production data is proposed. Using Well H flowback records, variable-production log-log well test plots and RNP-tm diagnostic charts were constructed for time-dependent fracturing effectiveness quantification. Key findings include: (1) Initial maximum cumulative water production derived from Arps harmonic decline model shows a semilogarithmic relationship between daily/cumulative water output; (2) Unit slope in fracturing fluid flowback indicates pseudosteady single-phase fracture depletion, while early positive slope deviation represents radial flow regime; (3) Complex fracture networks from stimulation reduce fluid seepage distances, transforming imbibition displacement into dominant mechanism and establishing fracture-dominated early flow imbibition-controlled sustained production progression. Field applications demonstrate the significance of flowback water production data in flow regime characterization and fracturing performance evaluation.**

**Keywords**: fracturing flowback data, flowback seepage, fracturing effectiveness evaluation, variable production conditions, unsteady well testing.

## 1 Introduction

After hydraulic fracturing, the subsurface fracture network becomes filled with fracturing fluid. During the shut-in stage, the fracturing fluid undergoes diffusion and displacement with oil and gas, and secondary fractures may extend. Once the shut-in period ends, flowback occurs. A large amount of flowback data can be used to evaluate the effectiveness of fracture stimulation. By analyzing early flowback or production data, the modification of effective fracture pore volume can be assessed, and production potential can be predicted. At present, research on the flowback process of hydraulic fracturing in tight reservoirs, both domestically and internationally, mainly focuses on three aspects: the mechanism of fracturing fluid

**Submitted:** 30 October 2025
**Accepted:** 10 March 2026
**Published:** 15 March 2026

**Vol.** 2, **No.** 2, 2026.
10.62762/RS.2026.228817

***Corresponding author:**
✉ Qiushi Zhang
zhangqiushi@lnpu.edu.cn

**Citation**
Tian, L., Zhang, Q., Li, X., & Li, C. (2026). Fracturing Effectiveness Evaluation Based on Flowback Data Using Pressure Transient Testing. *Reservoir Science*, 2(2), 97–110.

imbibition, the classification of flowback stages, and the evaluation of effective fracture pore volume after flowback.

Abbasi proposed a methodology for characterizing fractured horizontal wells through analysis of flowback fracturing fluid data [1]. This approach involves constructing a diagnostic plot between normalized pressure (RNP) and material balance time (MBT) to quantify fracture permeability values. Clarkson derived pre-breakthrough fracture permeability and fracture half-length by simulating the initial flowback regime of fracture pore volume - the single-phase depletion stage [2, 3]. Williams-Kovacs et al. [4] established an inversion-based analytical framework to extract fracture and reservoir parameters from production data. Fu et al. [5] evaluated fracture volume loss in Eagle Ford wells using fracture compressibility relationships, enabling estimation of effective fracture volume. Lin et al. [6] conducted post-fracturing model studies constrained by discrete fracture network (DFN) models and microseismic monitoring data, leading to the formulation of fracturing optimization protocols.

Wu et al. [7] simulated fracturing fluid injection dynamics through numerical modeling and developed a diagnostic technique for fracture property identification using shut-in pressure drawdown curves. Tang et al. [8] introduced a genetic algorithm (GA) workflow for shale gas EFNV inversion to characterize fracture network architectures. Xing et al. [9] formulated a well test interpretation model for vuggy carbonate reservoirs incorporating wellbore storage effects and skin factors, while analyzing the impact of vug parameters and fracture-to-reservoir ratios on well test signatures. Chu et al. [10] created a convolutional neural network (CNN)-based automated classification system for evaluating well test curve morphologies. Chen et al. [11] presented a well test interpretation methodology for multi-scale fracture-porous media, investigating pressure transient behaviors in naturally fractured gas reservoirs.

This study develops a multi-stage fractured horizontal well flowback seepage model by integrating transient fracture/matrix flow mechanisms with horizontal wellbore pressure loss. A fracturing performance evaluation model incorporating radial/linear flow regimes with aqueous phase mobility is established using material balance principles, with initial parameters including maximum cumulative production and fracture compressibility coefficient. The evaluation workflow comprises three steps: (1) wellhead casing pressure matching via flowback seepage model; (2) stage division based on choke size/fluid volume variations and dual-logarithmic pressure/derivative plot generation for each stage; (3) variable-rate well test diagnostic plot construction combining pressure/derivative responses with RNP-tm analysis to quantify effective fracture pore volume changes and fracture parameters. The proposed fracturing evaluation methodology offers significant methodological support for optimizing fracturing schemes during flowback operations.

## 2 Multi-stage Fractured Horizontal Well Seepage Flowback Model

### 2.1 Physical Model

Based on a complex fracture system, a physical model of a horizontally fractured well—comprising a single wellhead and a complex network of intersecting fractures—is constructed, as shown in Figure 1. In building this model, the following conditions must be satisfied [12]:

1. Horizontal, homogeneous, isotropic infinite reservoir;
2. Single-phase, homogeneous, slightly compressible fluid;
3. Fractures oriented perpendicular to formation;
4. Gravity and capillary forces neglected;
5. Fluid flow governed by Darcy's law;
6. Thermal effects on formation disregarded.

In this model, the horizontal wellbore is located at the center of the formation, with its edges parallel to the top and bottom boundaries of the formation. The fractures generated by hydraulic fracturing are perpendicular to the formation and intersect the wellbore at arbitrary angles. Meanwhile, the horizontal wellbore injects fluid into the formation at a constant injection rate and constant bottomhole pressure.

### 2.2 Unsteady Flow Model for Fractures

In the formation, an arbitrary small control volume is selected where no sources or sinks exist. In this case, the change in liquid phase mass within the closed surface of the control volume is equal to the difference between the mass of liquid flowing in and out over the same period of time [13].

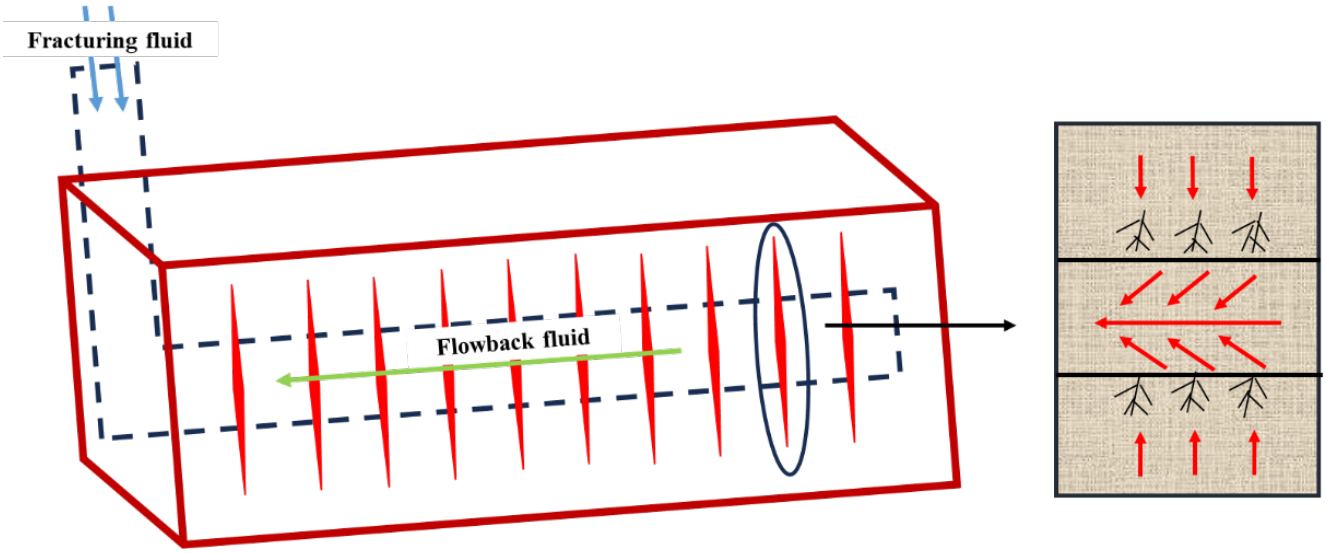


**Figure 1.** Physical model of a multi-stage fractured horizontal well.

The partial differential equation for fluid flow within the fracture is:

$$\frac{\partial^2 p_{fD}}{\partial x_D^2} + \frac{q_{fD}}{C_{fD}}(t_D) = \frac{1}{C_\eta}\frac{\partial p_{fD}}{\partial t_D}, \quad x_{D-1} \le x_D \le x_{Di} \tag{1}$$

In the equation: $p_{fD}$ is the dimensionless flow pressure in the fracture; $x_D$ is the dimensionless distance from the discrete point within the fracture; $q_{fD}$ is the dimensionless flow rate from the formation to each source point; $C_{fD}$ is the dimensionless conductivity; $t_D$ is the dimensionless time; and $C_\eta$ is the dimensionless diffusivity [14].

By applying the Laplace transform to the differential equation describing fluid flow within the fracture, the corresponding expression in the transformed domain can be obtained as follows [15]:

$$\frac{\partial^2 p_{fD}}{\partial x_D^2} - \frac{q_{fD}}{C_{fD}}(t_D) = \frac{1}{C_\eta} u p_{fD}, \quad x_{D-1} \le x_D \le x_{Di} \tag{2}$$

Since the flow rate within each element affects not only the two endpoints but also the pressure distribution throughout the entire element, the pressure at any point within the element can be expressed as:

$$\begin{aligned} p_{fD}(x_D, u) =& \bar{q}^*_{N_{Di-1}} \cdot p_s(x_D, x_{D-1}, u) \\ & - \bar{q}^*_{N_{Di}} \cdot p_s(x_D, x_{D_i}, u) - \frac{C_\eta}{C_{fD} u} q_{fDi} \end{aligned} \tag{3}$$

When analyzing the element, the boundaries at both ends are set as closed boundaries [16]. At point X, this point is treated as a line source. Based on this assumption, in Equation (3):

$$p_{fD}(x_D, u) = b_i(x_D)\, \bar{q}^*_{N_{Di-1}} - c_i(x_D)\, \bar{q}^*_{N_{Di}} + d_i q_{fDi} \tag{4}$$

where $q_{fDi}$ is the flow rate from the wellbore element into the formation.

$$\begin{aligned} b_i =& \frac{1}{C_{jD}\sqrt{u/C_\eta}} \frac{2\cosh\left((x_D - x_{D_{i-1}})\sqrt{u/C_\eta}\right)}{\exp\left(2(x_{D_i} - x_{D_{i-1}})\sqrt{u/C_\eta}\right)} \\ & + \exp\left(-|x_D - x_{D_{i-1}}|\sqrt{u/C_\eta}\right) \end{aligned} \tag{5}$$

$$\begin{aligned} c_i =& \frac{-1}{C_D\sqrt{\frac{u}{C_\eta}}} \frac{2\cosh\left[(x_D - x_{D_{i-1}})\frac{u}{\sqrt{C_\eta}}\right]}{\exp\left(2(X_{D_i} - X_{D_{i-1}}\sqrt{u/C_\eta})\right)} \\ & + \exp\left(-|x_D - x_{D_{i-1}}|\sqrt{\frac{u}{C_\eta}}\right) \end{aligned} \tag{6}$$

$$d_i = -\frac{C_\eta}{C_D u} \tag{7}$$

### 2.3 Unsteady Flow Model for the Formation

Based on the law of mass conservation, the unsteady-state continuity equation for slightly compressible fluids in a homogeneous and isotropic medium can be expressed as follows [17]:

$$-\left[\frac{\partial\left[\rho(p)v_x\right]}{\partial x}+\frac{\partial\left[\rho(p)v_y\right]}{\partial y}+\frac{\partial\left[\rho(p)v_z\right]}{\partial z}\right]=\frac{\partial\left[\phi\rho(p)\right]}{\partial t} \tag{8}$$

where $\rho$ is the fluid density ($\mathrm{kg/m^3}$), and $x, y, z$ are the spatial coordinates in three dimensions.

By organizing the above continuity, momentum, and state equations, the resulting differential equation is applicable to unsteady flow of single-phase, slightly compressible fluids:

$$\eta\left(\frac{\partial^2 p}{\partial x^2}+\frac{\partial^2 p}{\partial y^2}+\frac{\partial^2 p}{\partial z^2}\right)=\frac{\partial p}{\partial t} \tag{9}$$

When considering fluid flow in a two-dimensional space, the differential equation (Equation 8) can be transformed into:

$$\eta\left(\frac{\partial^2 p}{\partial x^2}+\frac{\partial^2 p}{\partial y^2}+\frac{\partial^2 p}{\partial z^2}\right)=\frac{\partial p}{\partial t} \tag{10}$$

where $r$ is the distance from a point in the formation to the center of the well, in meters (m).

By applying the Laplace transform [18], the dimensionless pressure variable $P_D$ is converted from the time domain, resulting in the following relationship between the dimensionless pressure $P_D$ and the time variable $t_D$:

$$\frac{\partial^2 \bar{P}_D}{\partial r_D^2}+\frac{1}{r_D}\frac{\partial \bar{P}_D}{\partial r_D}=u\cdot\bar{P}_D \tag{11}$$

Under constant production conditions, the internal boundary condition of the wellbore is:

$$\lim_{r_D\to 0}\left(r_D\frac{\partial \bar{P}_D}{\partial r_D}\right)=-\frac{\bar{q}_D}{u} \tag{12}$$

Under constant pressure conditions, the internal boundary condition of the wellbore is as follows:

$$\bar{P}_{wD}=\mathrm{cons\,tan}\,t/u \tag{13}$$

For an infinite formation, the external boundary condition is:

$$\bar{P}_D\left(+\infty,\,u\right)=0 \tag{14}$$

The general solution can be written as:

$$\bar{P}_D=AI_0\left(r\sqrt{u}\right)+BK_0\left(r\sqrt{u}\right) \tag{15}$$

$\lim_{x\to\infty} I_v(x)=\infty$,substituting into the equation gives $A=0$, and because $(x_1K_1(x))'=-x_1K_{v-1}$, $K_{-1}(x)=K_1(x)$, therefore:

$$\frac{\partial \bar{P}_D}{\partial r_D}=-BK_1\left(r_D\sqrt{u}\right)\sqrt{u} \tag{16}$$

According to the inner boundary condition and the above equation, we have:

$$\begin{aligned}\lim_{r_D\to 0}\left(r_D\frac{\partial \bar{P}_D}{\partial r_D}\right)&=\lim_{r_D\to 0}\left\{-\left[BK_1\left(r_D\sqrt{u}\right)r_D\sqrt{u}\right]\right\}\\&=-B\lim_{r_D\to 0}sK_1(s)=-B\end{aligned} \tag{17}$$

In the Laplace space, considering the pressure variation at an arbitrary point with wellbore storage effects, we have:

$$C_D u\bar{p}_{wD}-\left.\frac{\partial \bar{p}_D}{\partial r_D}\right|_{r_D=1}=\frac{1}{u} \tag{18}$$

On this basis, a method is proposed to express permeability differences using a dimensionless skin factor. When both the wellbore storage coefficient and the skin factor are considered in the Laplace space, the bottomhole flowing pressure can be expressed as:

$$\bar{p'}_{wD}(u)=\frac{u\bar{p}_{wD}+S}{u\left[1+C_D u\left(u\bar{p}_{wD}+S\right)\right]} \tag{19}$$

### 2.4 Pressure Drop Model for Horizontal Wellbores

The acceleration-induced pressure drop is primarily caused by changes in the kinetic energy of fluid particles, and this type of loss is most evident at the junction between the fracture and the wellbore [19]. The pressure drop loss can be expressed as:

$$7.45\times 10^{12}\frac{dp}{dx}=-\frac{d\left(\rho v_h^2\right)}{dx} \tag{20}$$

Substituting the fluid flow velocity in the wellbore into Equation 20 yields:

$$7.45\times 10^{12}\Delta p=\frac{4\rho}{\pi^2 r_w^4}\Delta q_w^2 \tag{21}$$

The pressures and flow rates before and after the intersection of the fracture and the wellbore are denoted as $P_{wi}$ and $P_{wi-1}$, and $q_{wi}$ and $q_{wi-1}$, respectively.

$$7.45 \times 10^{12} \left(p_{wi} - p_{wi-1}\right) = -\frac{4\rho_{sc}}{B\pi^2 r_w^4} q_{sc}^2 \left(q_{wi}^2 - q_{wi-1}^2\right) \tag{22}$$

The formation of frictional pressure drop is due to the roughness and irregularities on the inner wall of the wellbore during production, which causes a certain degree of friction as oil and gas flow. The expression for the frictional pressure drop is [20]:

$$7.45 \times 10^{12} \frac{dp}{dl} = -\frac{f\rho v_h^2}{4r_w} \tag{23}$$

In the equation, $l$ is the length of the line, in meters (m).

The magnitude of the friction factor $f$ depends on the fluid velocity during flow. When the fluid flow is in the laminar regime:

$$f = \frac{64}{N_{Re}} \tag{24}$$

When the fluid flow is in the turbulent regime:

$$f = 1/\left[1.17 - 2\log\left(R_p + \frac{21.25}{N_{Re}^{0.9}}\right)\right]^2 \tag{25}$$

In the equation, $R_p$ represents the relative roughness of the pipe wall.

## 3 Evaluation Model Based on Early Fracturing Fluid Flowback Data

### 3.1 Flow Characteristics of Fracturing Fluid During Flowback Stages

As shown in Figure 2 [21], studies have indicated that during the multi-stage fracturing flowback process of horizontal wells in shale and tight sandstone oil and gas reservoirs, three primary stages are commonly observed:

1. Early linear/radial flow stage: Fracturing fluid flows along primary fractures toward the wellbore. Upon breakthrough-induced radial flow, fracture permeability is derived from flowback data analysis;
2. Pseudo-steady flow stage: As flowback progresses, fracture pressure depletion propagates to the fracture-matrix interface. Effective fracture pore volume is calculated via fracture porosity-geometry coupling;
3. Unstable linear flow stage: Formation fluid influx creates biphasic flowback. Fracture half-length and matrix permeability are determined from this stage's flowback data.

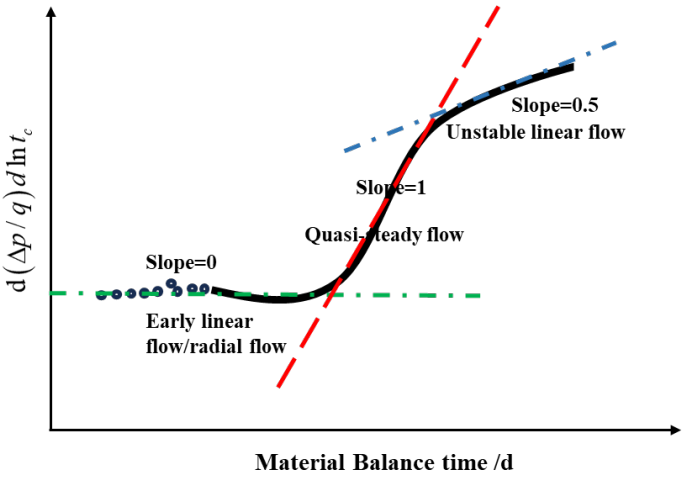


**Figure 2.** Characteristic flow stages during the flowback process.

### 3.2 Mathematical Model of Water Phase Seepage

#### *3.2.1 Material Balance Equation for the Water Phase*

During the fracturing fluid flowback process, the decline in formation pressure leads to two effects: expansion of the fluid volume and compression of the fracture pore volume due to increased effective stress in the formation. The elastic energy generated by these two deformation processes provides the driving force for the flowback fluid. Therefore, the volume of fracturing fluid flowing back from the effective fracture pore space constitutes the material balance equation for the water phase [22]. The cumulative flowback volume of fracturing fluid is equal to the sum of the expansion of formation fluid and the water phase, as well as the contraction of fracture pore volume caused by the drop in formation pressure, and can be expressed as:

$$q_w dt B_w = -dV_{EF} + dV_o + dV_w \tag{26}$$

where $V_{EF}$ is the effective fracture pore volume ($m^3$), $V_o$ is the oil phase volume ($m^3$), $V_w$ is the water phase volume ($m^3$), and $B_w$ is the formation volume factor of the water phase.

By substituting the isothermal compressibility

coefficients of oil, water, and rock into Equation (26), we obtain:

$$q_w dt B_w = -(V_{EF}C_f + V_o C_o + V_w C_w)dp \tag{27}$$

$C_w$, $C_o$, and $C_f$ are the isothermal compressibility coefficients of the water phase, oil phase, and rock, respectively, with units of 1/MPa [23].

Simplified as:

$$dp/dt = -q_w B_w / V_{EF} C_t \tag{28}$$

where $C_t = C_f + S_o C_o + S_w C_w$, By integrating Equation (3), we obtain:

$$B_w W_p = C_t V_{EF} \left(p_i - \overline{p}_f\right) \tag{29}$$

where $p_i$ is the initial reservoir pressure (MPa), $\overline{p}_f$ is the average reservoir pressure (MPa), and $C_t$ is the total compressibility coefficient (1/MPa).

### 3.2.2 *Radial Flow Model*

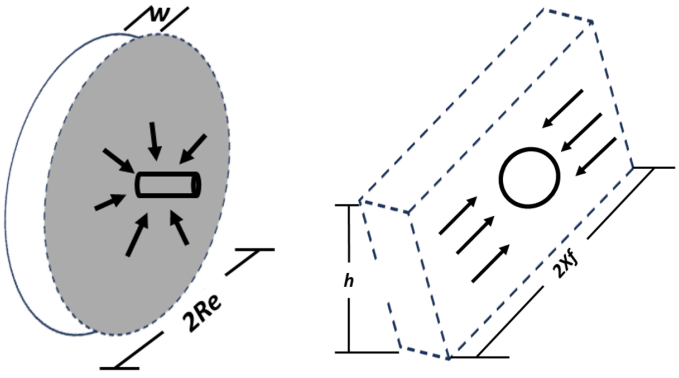


(a) Radial Flow Model (b) Linear Flow Model

**Figure 3.** Fracturing fluid flowback models [24].

Based on the model theory proposed by ABBASI, it is assumed that fluid flow within the fracture follows either radial or linear flow patterns. As shown in Figure 3(a), the water phase within the fracture flows into the wellbore in a radial manner, which is considered a radial flow model. When flowback occurs at a constant water production rate and reaches the boundary-dominated steady stage, the seepage flow mathematical model for the fracture is given by:

$$\frac{1}{r}\frac{\partial}{\partial r}\left(r\frac{\partial p_f}{\partial r}\right) = -\frac{q_w B_w \phi_f \mu}{K_f V_{EF}} \tag{30}$$

By substituting the boundary conditions of the wellbore and the fracture, we obtain:

$$p_f(r,t) = p_{wf}(t) + \frac{q_w B_w \phi_f \mu}{2K_f V_{EF}} R_e^2 \left(-\frac{r^2}{2R_e^2} + \ln\frac{r}{R_w}\right) \tag{31}$$

where $p_{wf}$ is the bottomhole flowing pressure (MPa); $K_f$ is the fracture permeability (mD); $\phi_f$ is the fracture porosity; $\mu$ is the water phase viscosity (MPa/s); $R_e$ is the fracture radius (m); $R_w$ is the wellbore radius (m); and $r$ is the radial flow distance (m).

The average fracture pressure in a circular fracture is:

$$\overline{p_f}(t) = \int_{R_w}^{R_e} p_f(r,t)\cdot 2\pi r\, dr \Big/ \pi(R_e^2 - R_w^2) \tag{32}$$

Substituting into Equation (32) and simplifying yields:

$$\overline{p_i} - p_{wf}(t) = \frac{q_w t B_w}{C_t V_{EF}} + \frac{q_w B_w \phi_f \mu}{2\pi K_f w}\left(\ln\frac{R_e}{R_w} - 0.75\right) \tag{33}$$

Equation (34) can be simplified as:

$$\frac{\overline{p_i} - p_{wf}(t)}{q_w} = \frac{t}{C_t V_{EF}} + \frac{B_w \phi_f \mu}{2\pi K_f w}\left(\ln\frac{R_e}{R_w} - 0.75\right) \tag{34}$$

### 3.2.3 *Linear Flow Model*

When the fracture flow stage is linear flow, the pressure distribution during the boundary-dominated stage is given by:

$$\frac{\partial^2 p_f}{\partial x^2} = -\frac{\phi_f \mu C_t}{K_f}\frac{B_w q_w}{C_t x_f w h} = -\frac{\phi_f \mu B_w q_w}{K_f V_{EF}} \tag{35}$$

By applying the boundary conditions of the wellbore and the fracture to the model, the solution is obtained as:

$$p_i - p_{wf}(t) = \frac{B_w q_w t}{V_{EF} C_t} + \frac{\phi_f \mu B_w q_w}{3K_f V_{EF}} x_f^2 \tag{36}$$

$x$ is the length in the fracture propagation direction (m); $h$ is the fracture height (m); and $x_f$ is the fracture half-length (m).

Rearranging Equation (37) yields:

$$\frac{p_i - p_{wf}(t)}{q_w} = \frac{t}{V_{EF} C_t} + \frac{\phi_f \mu B_w}{3K_f V_{EF}} x_f^2 \tag{37}$$

Define the production-normalized pressure as:

$$RNP = \frac{p_i - p_{wf}(t)}{q_w} \tag{38}$$

Pressure-normalized cumulative production:

$$PNR = \frac{1}{RNP} \tag{39}$$

The material balance time is:

$$t_m = \frac{W_p}{q_w} \tag{40}$$

RNP is the production-normalized pressure, in MPa/(m³/d); $t_m$ is the material balance time, in days (d).

### 3.3 Model Validation

Taking a domestic horizontal shale oil well H as an example, the stimulated interval of the well ranges from 1930 to 3500 meters, covering a total length of 1408 meters divided into 20 stages. A total of 118 clusters were fractured across the 20 stages. The designed proppant volumes include 760 $m^3$ of 0.212–0.106 mm quartz sand, 2054 $m^3$ of 0.425–0.212 mm quartz sand, and 707 $m^3$ of 0.85–0.425 mm quartz sand. The fracturing fluid used was a CNI nano-emulsion viscosity-modified slickwater system, with a design including 25 $m^3$ of acid fluid, 7525 $m^3$ of high-viscosity sand-carrying fluid, 6440 $m^3$ of low-viscosity sand-carrying fluid, and 13,584 $m^3$ of slickwater. A total of 762 dissolvable temporary plugging balls were designed. The historical data of fracturing fluid flowback is shown in Figure 4.

The calculation iterates as follows: initial maximum cumulative water production and fracture compressibility seed the process. RNP-$t_m$ dual-log derivative plots are constructed from flowback water production data to delineate flow regimes and identify unit-slope boundary-dominated pseudo-steady flow stages. Linear regression of pseudo-steady-state RNP-$t_m$ plots then provides iterative solutions for effective fracture pore volume through intercept matching [25].

By calculating the production-normalized pressure, its derivative, and the material balance time, a double logarithmic derivative plot is constructed. On this plot, characteristic curves corresponding to early radial flow, boundary-dominated flow, and unsteady linear flow are delineated [26]. As shown in Figure 5, there is a clearly identifiable pseudo-steady flow stage under boundary-dominated conditions.

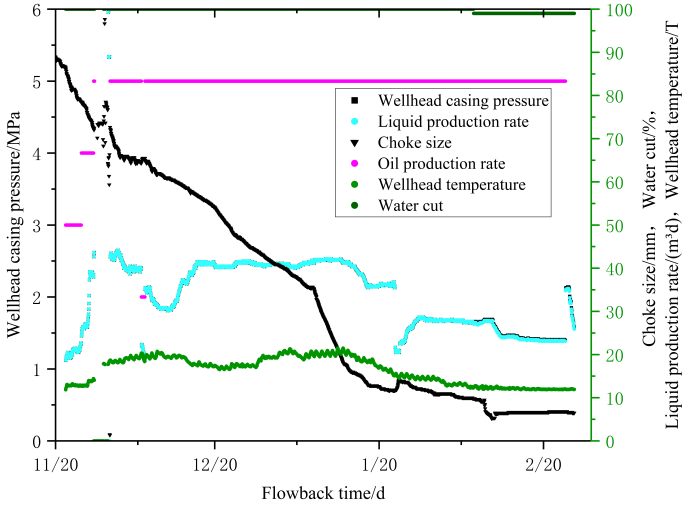


**Figure 4.** Historical flowback data of fracturing fluid for well H.

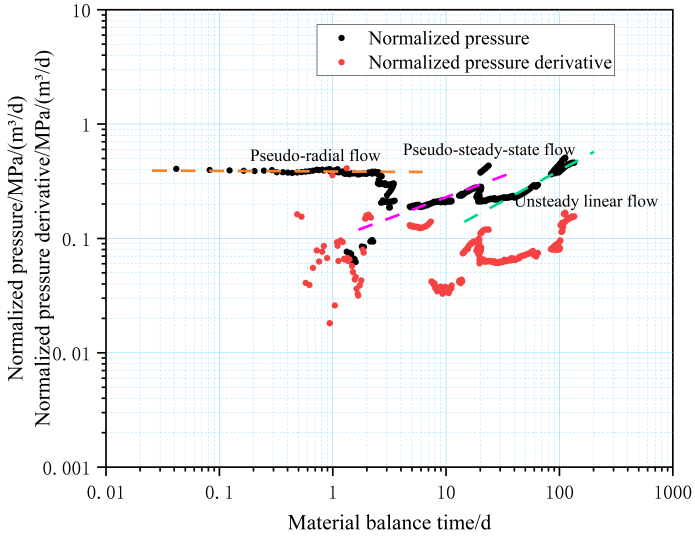


**Figure 5.** Double Logarithmic Derivative Plot of Production-Normalized Pressure vs. Material Balance Time.

Based on Figure 6, the curve of normalized production versus cumulative water production is obtained. The calculated effective fracture pore volume is 26,849.54m³, with a deviation of 6.86% from the maximum cumulative flowback volume. The calculated fracture compressibility coefficient is 0.01366$MPa^{-1}$, and the fracture half-length is 30.51m. These results demonstrate that the fracturing effectiveness evaluation model has good accuracy.

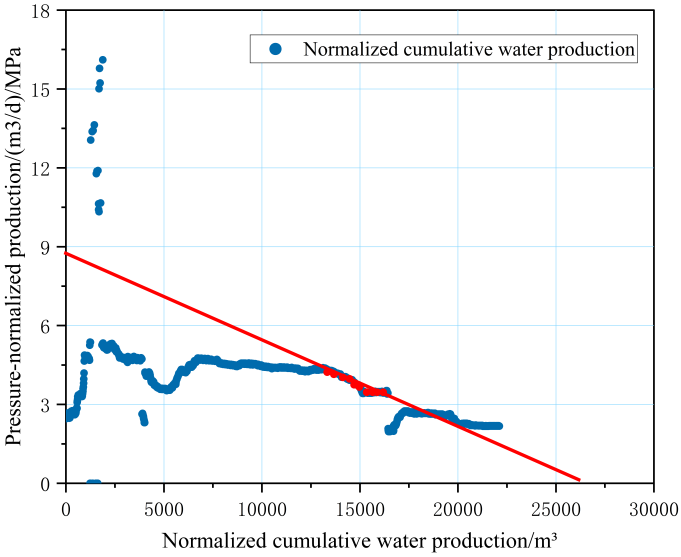


**Figure 6.** Pressure-Normalized Production vs. Normalized Cumulative Water Production Curve.

## 4 Fracturing Effectiveness Evaluation Based on the Seepage Flowback Mathematical Model

During the flowback stage, the choke size and flowback rate continuously change, making it a complex challenge to establish double logarithmic fitting plots at each time point to interpret the fluid flow patterns across different stages [27]. For complex conditions such as variable flow pressure or variable production rates, the entire variable production stage can be divided into several segments based on changes in flowback volume. It is then assumed that the production well operates at a constant production rate in each segment, and iterative calculations are performed using the principle of superposition [28].

According to the principle of superposition, the bottomhole pressure at time $t$ is equal to the sum of the pressure drops caused by each flowback rate $q_i$. The pressure drop at the bottomhole caused by $q_i$ under the $i$ operating condition can be expressed as:

$$\Delta p_i = \Delta p_i'(q_i, t - t_i) - \Delta p_i''(q_i, t - t_{i+1}) \tag{41}$$

As shown in Figure 7, the first part represents the pressure drop caused by the production rate $q_i$ from time $t_i$ to the current time $t$; the second part represents the pressure drop that would be generated by a hypothetical production rate of $q_i$ from the next time point $q_{i+1}$ to the current time $t$ [29]. The combined effect of these two parts serves to cancel out the impact of $q_i$ beginning at $t_{i+1}$. When multiple operating conditions exist, the total bottomhole pressure drop can be expressed as [30]:

$$\begin{aligned}\Delta p = \sum \Delta p_i = \\ \Delta p_0'(q_0, t) - \Delta p_0'(q_0, t - t_1) + \Delta p_1'(q_1, t - t_1) \\ - \Delta p_1''(q_1, t - t_2) + \cdots + \Delta p_{N-1}'(q_{N-1}, t - t_{N-1}) \\ - \Delta p_{N-1}''(q_{N-1}, t - t_N) + \Delta p(q_N, t - t_N)\end{aligned} \tag{42}$$

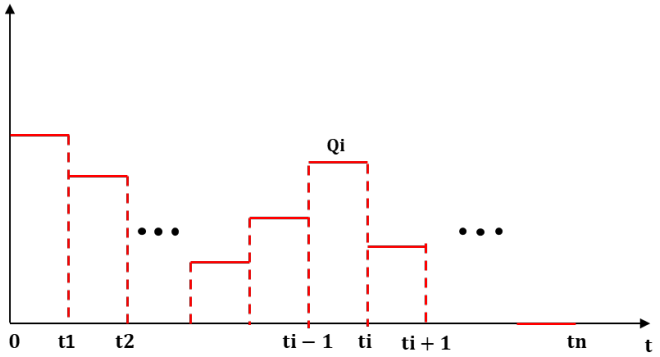


**Figure 7.** Schematic diagram of variable production rate changes.

In this section, starting from the shut-in flowback time, double logarithmic derivative plots are generated under different permeability values (0.05, 0.1, 0.5) while keeping other physical properties constant, and varying the number of fractures (4, 8, 12, 16, 20). These plots are fitted with the actual wellhead casing pressure data, and combined with the RNP-$t_m$ double logarithmic plots to quantitatively evaluate the fracturing flowback effectiveness and the variation patterns of fracture parameters.

### 4.1 Double Logarithmic Plots for Different Numbers of Fractures Under Varying Permeabilities

As shown in Figure 8, distinct flow stages are observed. The double logarithmic well test interpretation plot for the entire flowback process can be divided into the following stages [31]: (1)Wellbore Storage and Skin Effect Stage: At the initial moment, the pressure and pressure derivative curves coincide and exhibit a unit slope (slope=1); subsequently, under the influence of the skin effect, the two curves separate, and the pressure derivative curve displays a hump-shaped pattern. (2)Fracture Bilinear Flow Stage: During this stage, fluid flows from the matrix into the main fracture, while linear flow occurs within the main fracture. The pressure curve and the pressure derivative curve run parallel, with the slope decreasing to 1/4. (3) Linear Flow Stage: In this stage, linear flow within the main

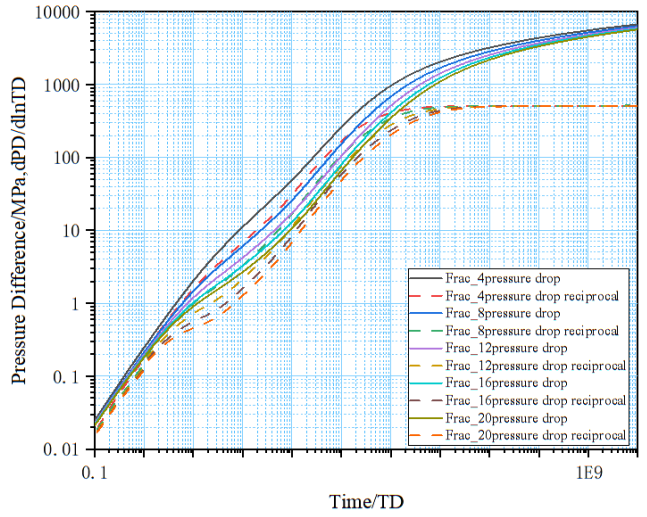


（a）k=0.05md

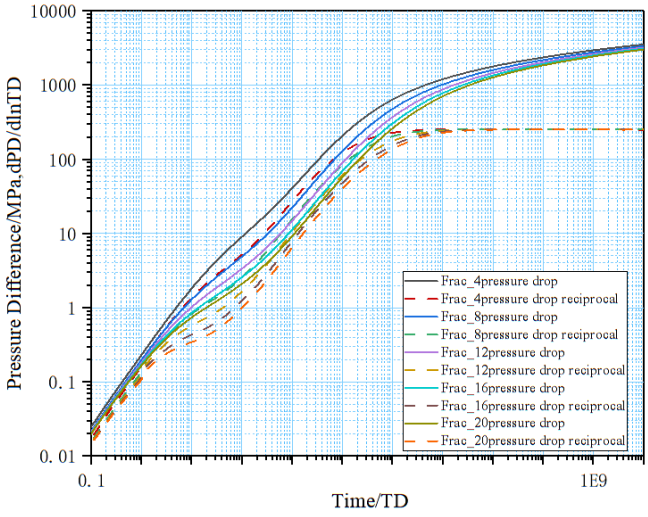


（b）k=0.1md

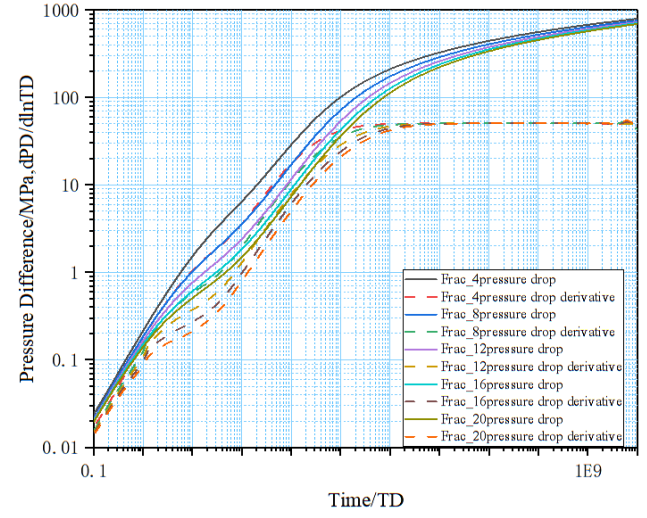


（c）k=0.5md

**Figure 8.** Double Logarithmic Derivative Plots for Different Numbers of Fractures at Various Permeabilities.

fracture reaches a relatively stable state, and the slope of the pressure derivative curve increases to 1/2. (4) Pseudo-Steady-State Stage: When the pressure wave reaches the boundary, the system enters the pseudo-steady-state flow stage. The pressure response characteristics during this stage reflect the geometric dimensions and boundary conditions of the stimulated reservoir volume, providing key information for evaluating the fracturing effectiveness.

As the number of fractures increases, both the pressure and pressure derivative curves exhibit an overall downward shift. The influence of fracture number on the double logarithmic curves is mainly concentrated in the early and middle stages. Once the radial flow stage is reached, the impact of fracture number on the curve shape becomes less significant. This is because the interference between fractures intensifies with increasing fracture density, causing the characteristic horizontal line of the radial flow stage to become progressively blurred or even disappear.

During the flowback process, the bottomhole flowing pressure fluctuates continuously. This dynamic change leads to a gradual reduction in effective fracture volume. Under the combined influence of bottomhole pressure and proppant, the fracture closure rate decreases as flowback time increases. A further comparison of formations with different permeabilities over the same time period reveals that as reservoir permeability increases, the flow efficiency of the fracturing fluid improves, the pressure decline during flowback accelerates, and fracture closure occurs more rapidly, resulting in a further reduction of the effective fracture volume. Therefore, when performing fracturing treatments in high-permeability reservoirs, special attention should be paid to the potential impact of reduced SRV (Stimulated Reservoir Volume) on production. Increasing the proppant concentration can help optimize fracture closure control during the flowback stage.

### 4.2 Evaluation of Fracturing Effectiveness at Different Time Periods

#### *4.2.1 Time Period: December 20 – January 8*

During this time period, continuous flowback was conducted using a 5mm choke, with an average flowback rate of 58.9m³/d. Double logarithmic well test plots under variable production conditions were established for different permeabilities and varying numbers of fractures. At a permeability of 0.1, the actual pressure drop and its derivative were fitted.

As shown in Figure 9, the pressure decline during

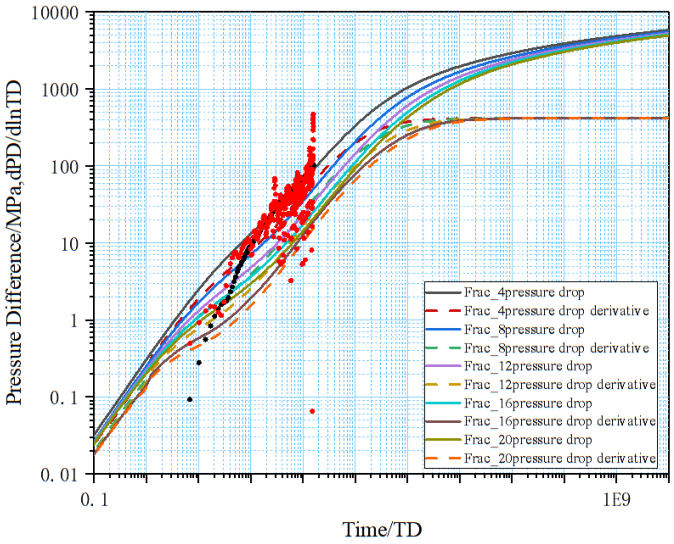


(a) Double Logarithmic Derivative Plot Fitted with Wellhead Casing Pressure

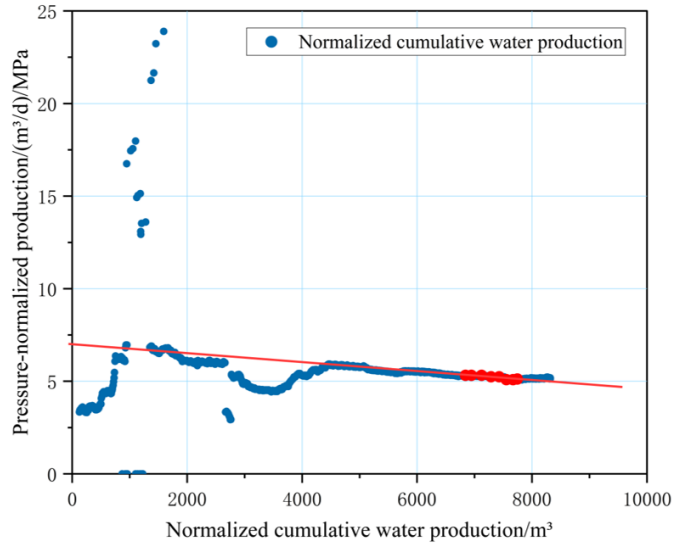


(b) *RNP-$t_m$* Double Logarithmic Plot

**Figure 9.** Fracturing Effectiveness Evaluation Chart for the December 20 – January 8 Time Period.

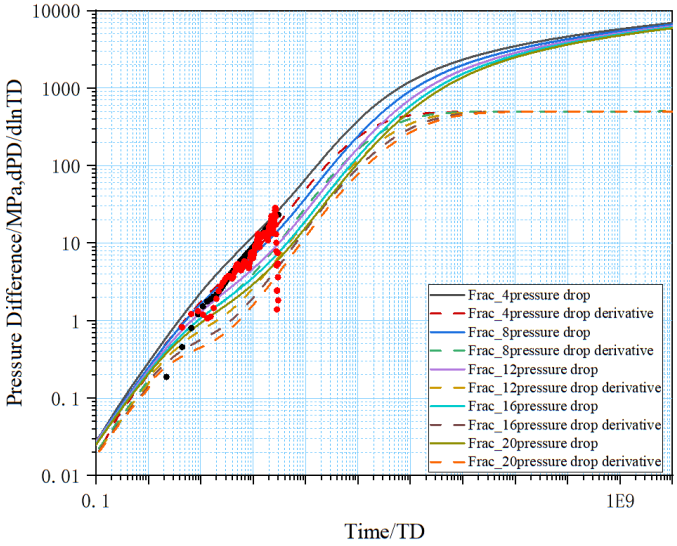


(a) Double Logarithmic Derivative Plot Fitted with Wellhead Casing Pressure

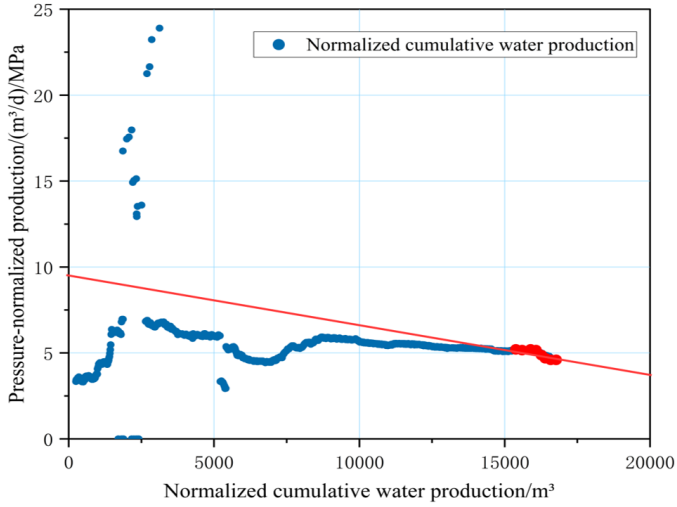


(b) *RNP-$t_m$* Double Logarithmic Plot

**Figure 10.** Fracturing Effectiveness Evaluation Chart for the January 8 – January 14 Time Period.

this time period slows down, and the flowback rate stabilizes around 60m³/d. The calculated effective fracture pore volume is 34,658.14m³, indicating that the fractures contain sufficient energy.

### *4.2.2 Time Period: January 8 – January 14*

During this time period, continuous flowback was conducted using a 5mm choke, with an average flowback rate of 60 m³/d. Double logarithmic well test plots under variable production conditions were generated for different permeabilities and varying numbers of fractures. At a permeability of 0.1, the actual pressure drop and its derivative were fitted.

As shown in Figure 10, the wellhead casing pressure drops rapidly during this stage, and the fracture pore volume increases to 36,723.73m³, indicating improved fracture opening and proximity to the controlled boundary, reaching the maximum effective fracture pore volume.

### *4.2.3 Time Period: January 14 – January 24*

During this time period, continuous flowback was conducted using a 5mm choke, with an average flowback rate of 53.6m³/d. At 13:00 on January 23, the balance valve was opened to control the liquid rate, resulting in a decrease in flowback from 50m³/d to 30m³/d. Between 06:00 on January 8 and 07:00 on January 12, the pressure dropped rapidly, while from January 12 to January 24, a brief pressure recovery occurred. Double logarithmic well test plots under

variable production conditions were established for different permeabilities and fracture counts, and the actual pressure drop and its derivative were fitted at a permeability of 0.1.

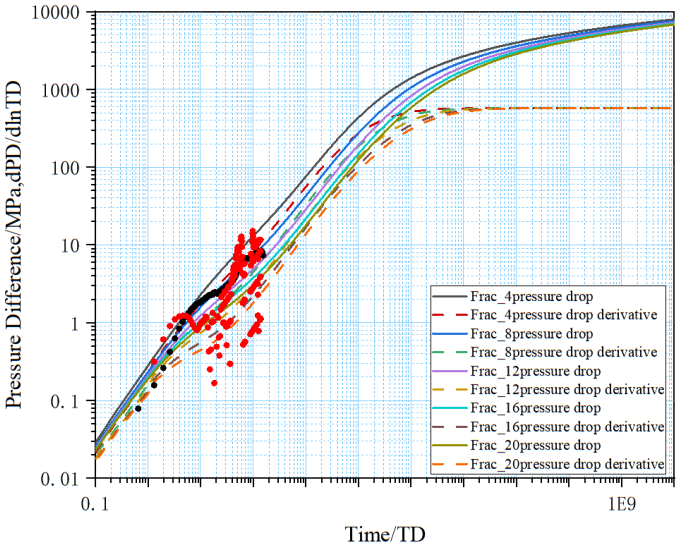


(a) Double Logarithmic Derivative Plot Fitted with Wellhead Casing Pressure

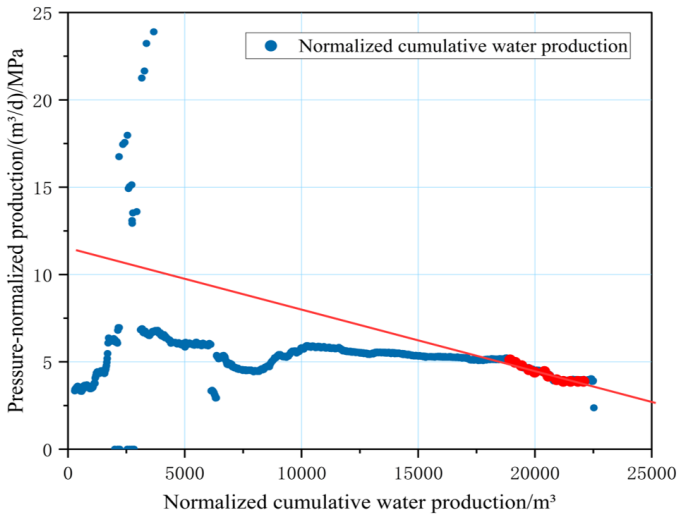


(b) *RNP*-$t_m$ Double Logarithmic Plot

**Figure 11.** Fracturing Effectiveness Evaluation Chart for the January 14 – January 24 Time Period.

As shown in Figure 11, during this stage, the pressure drop slows down, the flowback rate decreases to 51.5m³/d, and the effective fracture pore volume reduces to 31,981.28m³, indicating that the system has entered a boundary-dominated pseudo-steady flow stage, and the fractures are gradually closing.

### 4.3 Analysis and Discussion

Case H analysis: Flowback history shows 5.55MPa shut-in casing pressure, with 3mm→5mm choke progression during water-dominated flowback. Initial water production (28,691.721m³) derived via semi-log correlation with normalized production. Arps harmonic decline model ($R^2$=0.9000) validates initial effective fracture volume calculation. Flow regimes (early radial/unstable linear/pseudo-steady flow) identified through dual-log derivative plots. Linear RNP-MBT correlation established for pseudo-steady phase (m=0.0028 slope), enabling effective fracture pore volume and fracture parameter determination from production-cumulative water plots [32].

In the division of flow stages, a unit slope characterizes the pseudo-steady-state flow stage of single-phase fracture depletion, during which the fracturing fluid is primarily produced from the fractures, and production from the matrix is negligible [33]. In the early stage of flowback, a positive deviation occurs due to instantaneous radial flow of the water phase within the fractures; during this phase, fracture permeability is significantly higher than that of the matrix, and the duration is short. As the energy of the single-phase fracturing fluid is depleted, the boundary responses of fractures at different scales become uniform, and the system enters the boundary-dominated flow stage. When the fracture response deviates from the unit slope and a negative deviation appears, it signifies hydrocarbon breakthrough and the transition to unsteady linear flow.

In terms of the evolution of the driving mechanism, the pressure buildup effect during the shut-in stage causes the fractures to store water primarily in the early phase, while oil and gas production from the horizontal well remains extremely low, resulting in an extremely high water cut in the flowback fluid. Most fracturing fluid loss occurs during the early stage of flowback, with negligible losses in the later stages. The driving mechanism exhibits a dynamic transition: in the early flowback stage, fracture closure is the dominant mechanism, while after hydrocarbon breakthrough, fluid expansion gradually becomes the primary factor controlling fracture closure. The complex fracture system formed by SRV fracturing reconfigures the reservoir seepage pathways, shortening the flow distance and enhancing fluid exchange between the fractures and matrix. This transforms imbibition displacement from a secondary to a primary recovery mechanism. SRV results show that matrix pore imbibition contributes up to 93.14%, highlighting its critical role in the development of unconventional oil and gas reservoirs and forming a progressive pattern of fracture-dominated early flow

and imbibition-controlled long-term production.

## 5 Conclusions

This paper establishes a seepage flowback model for multi-stage fractured horizontal wells and a fracturing effectiveness evaluation model based on material balance principles. Through fitting of wellhead casing pressure charts, double-logarithmic well test charts of pressure drawdown derivatives under variable production rate conditions, and normalized pressure charts, the following conclusions are drawn:

1. A seepage flowback mathematical model was established based on the theories of unsteady fracture flow and unsteady formation flow in multi-stage fractured horizontal wells, incorporating a coupled vertical wellbore gas-liquid two-phase flow model and a horizontal wellbore pressure drop model. Additionally, a fracturing effectiveness evaluation model based on flowback data was developed using the material balance method, which includes both radial and linear flow models.

2. The fracturing effectiveness evaluation model was validated through a case study: by calculating the production-normalized pressure, its derivative, and material balance time, an RNP-$t_m$ double logarithmic derivative plot was constructed. In this plot, characteristic curves for radial flow, linear flow, and pseudo-steady-state flow were identified. The pseudo-steady-state stage with a unit slope was fitted, and the slope of the straight line was obtained. A curve of normalized production versus cumulative water production was then generated, from which the effective fracture pore volume and fracture parameters were ultimately calculated.

3. Based on the flowback data from Well H, double logarithmic derivative plots of fitted casing pressure were constructed for variable production conditions with different permeabilities and numbers of fractures using the principle of pressure superposition. Combined with the RNP-$t_m$ double logarithmic derivative plots, the fracturing effectiveness was quantitatively evaluated.

## Data Availability Statement

Data will be made available on request.

## Funding

This work was supported by the Liaoning Provincial Department of Science and Technology, China, under Grant 2023JH2/10700020, and by the Liaoning Provincial Department of Science and Technology, China, under Grant JYTNS20231443.

## Conflicts of Interest

Xingcai Li is affiliated with the China Petroleum Group Great Wall Drilling Engineering Co., Ltd., Liaoning, China. The authors declare that this affiliation had no influence on the study design, data collection, analysis, interpretation, or the decision to publish, and that no other competing interests exist.

## AI Use Statement

The authors declare that no generative AI was used in the preparation of this manuscript.

## Ethical Approval and Consent to Participate

Not applicable.

## References

[1] Abbasi, M. A., Dehghanpour, H., & Hawkes, R. V. (2012, October). Flowback analysis for fracture characterization. In *SPE Canada Unconventional Resources Conference* (pp. SPE-162661). SPE. [CrossRef]

[2] Clarkson, C. R., & Williams-Kovacs, J. D. (2013). Modeling two-phase flowback of multifractured horizontal wells completed in shale. *SPE Journal*, *18*(4), 795-812. [CrossRef]

[3] Clarkson, C. R., & Williams-Kovacs, J. D. (2013, September). A new method for modeling multi-phase flowback of multi-fractured horizontal tight oil wells to determine hydraulic fracture properties. In *SPE Annual Technical Conference and Exhibition?* (p. D031S041R007). SPE. [CrossRef]

[4] Williams-Kovacs, J. D., Clarkson, C. R., & Zanganeh, B. (2015, October). Case studies in quantitative flowback analysis. In *SPE Canada Unconventional Resources Conference* (p. D011S003R004). SPE. [CrossRef]

[5] Fu, Y., Dehghanpour, H., Motealleh, S., Lopez, C. M., & Hawkes, R. (2019). Evaluating fracture volume loss during flowback and its relationship to choke size: fastback vs. slowback. *SPE Production & Operations*, *34*(03), 615-624. [CrossRef]

[6] Lin, Y., Liu, S., Gao, S., Yuan, Y., Wang, J., & Xia, S. (2021). Study on the optimal design of volume fracturing for shale gas based on evaluating the fracturing effect—A case study on the Zhao Tong shale gas demonstration zone in Sichuan, China. *Journal of*

*Petroleum Exploration and Production, 11*(4), 1705-1714. [CrossRef]

[7] Wu, J., Ren, L., Chang, C., Sheng, S., Zhu, J., Liu, S., ... & Wang, F. (2024). Diagnostics of Secondary Fracture Properties Using Pressure Decline Data during the Post-Fracturing Soaking Process for Shale Gas Wells. *Processes, 12*(2), 239. [CrossRef]

[8] Tang, D., Wu, J., Zhao, J., Zeng, B., Song, Y., Shen, C., ... & Wang, Z. (2024). The Inversion Method of Shale Gas Effective Fracture Network Volume Based on Flow Back Data—A Case Study of Southern Sichuan Basin Shale. *Processes, 12*(5), 1027. [CrossRef]

[9] Xing, C., Yin, H., Liu, K., Li, X., & Fu, J. (2018). Well test analysis for fractured and vuggy carbonate reservoirs of well drilling in large scale cave. *Energies, 11*(1), 80. [CrossRef]

[10] Chu, H., Liao, X., Dong, P., Chen, Z., Zhao, X., & Zou, J. (2019). An automatic classification method of well testing plot based on convolutional neural network (CNN). *Energies, 12*(15), 2846. [CrossRef]

[11] Chen, D., Wang, X., Yang, F., Chang, B., Liu, L., Wang, J., & Zhou, W. (2024). Pressure transient test analysis for deep fractured gas reservoirs in Tarim Basin. *Energies, 17*(7), 1717. [CrossRef]

[12] Zhang, Q., Wang, X., Wang, D., Zeng, J., Zeng, F., & Zhang, L. (2018). Pressure transient analysis for vertical fractured wells with fishbone fracture patterns. *Journal of Natural Gas Science and Engineering, 52*, 187-201. [CrossRef]

[13] Wang, S., Zhou, J., Zhang, L., Wang, Y., & Chen, T. (2024). Numerical insight into hydraulic fracture propagation in hot dry rock with complex natural fracture networks via fluid-solid coupling grain-based modeling. *Energy, 295*, 131060. [CrossRef]

[14] Wan, Y., Liu, Y., Chen, F., Wang, J., & Li, Z. (2018). Numerical well test model for caved carbonate reservoirs and its application in Tarim Basin, China. *Journal of Petroleum Science and Engineering, 161*, 611-624. [CrossRef]

[15] Zhang, Q., Wang, D., Zeng, F., Guo, Z., & Wei, N. (2020). Pressure transient behaviors of vertical fractured wells with asymmetric fracture patterns. *Journal of Energy Resources Technology, 142*(4), 043001. [CrossRef]

[16] Wang, B., Zhang, Q., Yao, S., Zeng, F., & Wang, D. (2022). A semi-analytical mathematical model for the pressure transient analysis of multiple fractured horizontal well with secondary fractures. *Journal of Petroleum Science and Engineering, 208*, 109444. [CrossRef]

[17] Li, N., Yang, K., & Kao, J. (2023). A new extended finite element model for gas flow in shale gas reservoirs with complex fracture networks. *Arabian Journal of Geosciences, 16*(9), 519. [CrossRef]

[18] Qin, J., Xu, Y., Tang, Y., Liang, R., Zhong, Q., Yu, W., & Sepehrnoori, K. (2022). Impact of complex fracture networks on rate transient behavior of wells in unconventional reservoirs based on embedded discrete fracture model. *Journal of Energy Resources Technology, 144*(8), 083007. [CrossRef]

[19] Chen, Y., Zhang, Q., Zhao, Z., Wang, L., & Liu, H. (2022). Semi-analytical model for the transient analysis of the pressure in vertically fractured wells in reservoirs considering the influence of natural fractures. *Journal of Energy Resources Technology, 144*(8), 083005. [CrossRef]

[20] Jiaming, Z., Zongxiao, R., Guiyi, Z., Zhenhua, P., Minjing, C., Liang, W., ... & Xinggang, M. (2022). Study on flow model of multi-stage fracturing horizontal well in stress-denpendent dual medium reservoir. *Frontiers in Earth Science, 10*, 990684. [CrossRef]

[21] Abbasi, M. A., Ezulike, D. O., Dehghanpour, H., & Hawkes, R. V. (2014). A comparative study of flowback rate and pressure transient behavior in multifractured horizontal wells completed in tight gas and oil reservoirs. *Journal of Natural Gas Science and Engineering, 17*, 82-93. [CrossRef]

[22] Wang, Y., Lei, Z., Xu, Z., Liu, J., Zhang, X., Luo, E., ... & Liu, P. (2021). A Novel Mathematical Model for Fracturing Effect Evaluation Based on Early Flowback Data in Shale Oil Reservoirs. *Geofluids, 2021*(1), 1780937. [CrossRef]

[23] Chen, Q., Wang, S., Zhu, D., Ren, G., Zhang, Y., & Hu, J. (2020). A comprehensive model for estimating stimulated reservoir volume based on flowback data in shale gas reservoirs. *Geofluids, 2020*(1), 8886988. [CrossRef]

[24] Williams-Kovacs, J. D., & Clarkson, C. R. (2013, November). Stochastic modeling of multi-phase flowback from multi-fractured horizontal tight oil wells. In *SPE Canada Unconventional Resources Conference* (pp. SPE-167232). SPE. [CrossRef]

[25] Xiao, J., Ke, X., & Wu, H. (2021). Production decline analysis and hydraulic fracture network interpretation method for shale gas with consideration of fracturing fluid flowback data. *Geofluids, 2021*(1), 6076566. [CrossRef]

[26] Liao, K., Zhu, J., Sun, X., Zhang, S., & Ren, G. (2022). Numerical investigation on injected-fluid recovery and production performance following hydraulic fracturing in shale oil wells. *Processes, 10*(9), 1749. [CrossRef]

[27] Zhang, F., & Emami-Meybodi, H. (2020). Flowback fracture closure of multi-fractured horizontal wells in shale gas reservoirs. *Journal of Petroleum Science and Engineering, 186*, 106711. [CrossRef]

[28] Liu, S., Cao, N., Lou, Y., & Yuan, Y. (2023). A new approach for post-fracturing evaluation and productivity prediction based on a reservoir fracability index model in shale gas reservoirs. *Journal of Petroleum Exploration and Production Technology, 13*(8), 1807-1818. [CrossRef]

[29] Huang, Y., Li, X., Guo, W., Liu, X., Lin, W., Qian, C., ... & Shi, X. (2023). Research on productivity evaluation method based on shale gas well early flow stage data. *Geofluids, 2023*(1), 2529837. [CrossRef]

[30] Zhang, Q., Wang, B., Chen, W., Wang, W., & Zeng, F. (2021). Pressure transient analysis of vertically fractured wells with multi-wing complex fractures. *Petroleum Science and Technology, 39*(9-10), 323-350. [CrossRef]

[31] Ren, L., Dou, M., Dong, X., Chen, B., Zhang, L., Sun, J., ... & Li, H. (2024). Quantitative characterization of stimulated reservoir volume (SRV) fracturing effects in naturally fractured unconventional hydrocarbon reservoirs. *Frontiers in Earth Science, 12*, 1419631.

[32] Kang, L., Wang, G., Zhang, X., Guo, W., Liang, B., Jiang, P., ... & Sun, Y. (2024). Dynamic pressure analysis of shale gas wells considering three-dimensional distribution and properties of the hydraulic fracture network. *Processes, 12*(2), 286. [CrossRef]

[33] Li, L., YaWan, T., Aiwei, Z., Qian, Z., Yimin, W., & Jin, C. (2024). New approach of evaluating fracturing interference based on wellhead pressure monitoring data: a case study from the well group-A of Fuling shale gas field. *Journal of Petroleum Exploration and Production Technology, 14*(1), 139-148. [CrossRef]